SAND REPORT

SAND2002-0482
Unlimited Release
Printed February 2002

An Evaluation of the Material Point Method

Zhen Chen and Rebecca Brannon

Prepared by
Sandia National Laboratories
Albuquerque, New Mexico 87185 and Livermore, California 94550

Sandia is a multiprogram laboratory operated by Sandia Corporation, a Lockheed Martin Company, for the United States Department of Energy under Contract DE-AC04-94AL85000.

Issued by Sandia National Laboratories, operated for the United States Department of Energy by Sandia Corporation.

Available to DOE and DOE contractors from
U.S. Department of Energy
Office of Scientific and Technical Information
P.O. Box 62
Oak Ridge, TN 37831

Telephone: (865)576-8401
Facsimile: (865)576-5728
E-Mail: reports@adonis.osti.gov
Online ordering: http://www.doe.gov/bridge

Available to the public from
U.S. Department of Commerce
National Technical Information Service
5285 Port Royal Rd
Springfield, VA 22161

Telephone: (800)553-6847
Facsimile: (703)605-6900
E-Mail: orders@ntis.fedworld.gov
Online order: http://www.ntis.gov/ordering.htm

SAND2002-0482
Unlimited Release
Printed February 2002

An Evaluation of the Material Point Method

Zhen Chen
Department of Civil and Environmental Engineering
University of Missouri-Columbia
Columbia, MO 65211-2200

Rebecca Brannon
Department of Materials Mechanics
Sandia National Laboratories
PO Box 5800
Albuquerque, NM 87185-0893

Abstract

The theory and algorithm for the Material Point Method (MPM) are documented, with a detailed discussion on the treatments of boundary conditions and shock wave problems. A step-by-step solution scheme is written based on direct inspection of the two-dimensional MPM code currently used at the University of Missouri-Columbia (which is, in turn, a legacy of the University of New Mexico code). To test the completeness of the solution scheme and to demonstrate certain features of the MPM, a one-dimensional MPM code is programmed to solve one-dimensional wave and impact problems, with both linear elasticity and elastoplasticity models. The advantages and disadvantages of the MPM are investigated as compared with competing mesh-free methods. Based on the current work, future research directions are discussed to better simulate complex physical problems such as impact/contact, localization, crack propagation, penetration, perforation, fragmentation, and interactions among different material phases. In particular, the potential use of a boundary layer to enforce the traction boundary conditions is discussed within the framework of the MPM.

Acknowledgement

The authors appreciate the computing assistance by Mr. Luming Shen at the University of Missouri-Columbia, and the comments and suggestions from the reviewers.

Sandia is a multiprogram laboratory operated by Sandia Corporation, a lock heed martin Company, for the United States Department of Energy under Contract DE-ALO4-94AL8500.

Contents

1. Introduction

Throughout the last few decades, several kinds of "meshless" methods for spatial discretization have been proposed in the computational mechanics community. Because these "meshless" methods do not use a rigid mesh connectivity as compared with the conventional mesh-based methods such as FEM, FDM and BEM, they have been applied to some complex problems of current interests such as impact/contact, localization, crack propagation, penetration, perforation and fragmentation. Although academic exercises have demonstrated the robustness and potential of these "meshless" methods, they have not found their way successfully into general practical applications due to some unsolved problems such as boundary treatments, large rotation, and interactions among different material phases. The fact that no consensus has been made on the formal name of this type of method reflects the controversy involved in the development of any innovative approach for simulating the above-mentioned complex problems.

As one of the most straightforward spatial discretization methods, the Material Point Method (MPM) is an extension to solid mechanics problems of a hydrodynamics code called FLIP which, in turn, evolved from the Particle-in-Cell Method dating back to the pioneering work of Harlow [1964]. The motivation of the development was to simulate problems such as impact/contact, penetration and perforation with history-dependent internal state variables, as advocated in several important publications about the MPM [Sulsky et al., 1994 and 1995; Sulsky and Schreyer, 1996]. The essential idea is to take advantage of both the Eulerian and Lagrangian methods, which can be summarized as follows.

1.1 Governing Equations of Continuum

For a continuum under purely mechanical loading, the governing differential equations can be derived from the conservation equation for mass,

$$\frac{d\rho}{dt} + \rho \nabla \cdot \boldsymbol{v} = 0 \tag{1-1}$$

and the conservation equation for momentum,

$$\rho \boldsymbol{a} = \nabla \cdot \boldsymbol{s} + \rho \boldsymbol{b} \tag{1-2}$$

supplemented with a suitable constitutive equation, and kinematic relation between strain and displacement. In Eqs. (1-1) and (1-2), $\rho(\boldsymbol{x},t)$ is the mass density, $\boldsymbol{v}(\boldsymbol{x},t)$ is the velocity, $\boldsymbol{a}(\boldsymbol{x},t)$ is the acceleration, $\boldsymbol{s}(\boldsymbol{x},t)$ is Cauchy stress tensor, and $\boldsymbol{b}(\boldsymbol{x},t)$ is the specific body force. The vector $\boldsymbol{x}$ is the current position at time t of any material point in the continuum. For given boundary and initial data, the governing differential equations can be solved either analytically or numerically, if they are well-posed. The key difference among different spatial discretization methods is the way in which the gradient and divergence terms are calculated.

1.2 Discrete Forms of the Governing Equations

The MPM discretizes a continuum body with the use of a finite set of N_p material points in the original configuration that are tracked throughout the deformation process. Let $\boldsymbol{x}_p^t$ ($p = 1,2,...,N_p$) denote the current position of material point p at time t. Each material point at time t has an associated mass M_p, density ρ_p^t, velocity $\boldsymbol{v}_p^t$, Cauchy stress tensor $\boldsymbol{s}_p^t$, strain $\boldsymbol{e}_p^t$, and any other internal state variables necessary for the constitutive model. Thus, these material points provide a Lagrangian description of the continuum body. Since each material point contains a fixed amount of mass for all time, Eq. (1-1) is automatically satisfied. At each time step, the information from the material points is mapped to a background computational mesh (grid). This mesh covers the computational domain of interest, and is chosen for computational convenience. After the information is mapped from the material points to the mesh nodes, the discrete formulation of Eq. (1-2) can be obtained on the mesh nodes, as described below.

The weak form of Eq. (1-2) can be found, based on the standard procedure used in the FEM [see, for example, Sulsky et al., 1994 and 1995; Sulsky and Schreyer, 1996], to be

$$\int_\Omega \rho \boldsymbol{w}\cdot\boldsymbol{a}\,d\Omega = -\int_\Omega \rho \boldsymbol{s}^{\boldsymbol{s}} : \nabla \boldsymbol{w}\,d\Omega + \int_{S^c} \rho \boldsymbol{c}^{s}\cdot\boldsymbol{w}\,dS + \int_\Omega \rho \boldsymbol{w}\cdot\boldsymbol{b}\,d\Omega \qquad (1\text{-}3)$$

in which $\boldsymbol{w}$ denotes the test function, $\boldsymbol{s}^{\boldsymbol{s}}$ is the specific stress (i.e., stress divided by mass density, $\boldsymbol{s}^{\boldsymbol{s}} = \boldsymbol{s}/\rho$), Ω is the current configuration of the continuum, S^c is that part of the boundary with a prescribed traction, and $\boldsymbol{w}$ is assumed to be zero on the boundary

with a prescribed displacement. To our knowledge, no MPM code has yet been written that supports nonzero tractions on a moving boundary. Below, we will introduce the concept of a boundary layer to enforce the moving traction boundary condition with the use of the specific traction vector $\boldsymbol{c}^{\boldsymbol{s}}$ (i.e., traction divided by mass density).

Since the whole continuum body is described with the use of a finite set of material points (mass elements), the mass density can be written as

$$\rho(\boldsymbol{x},t) = \sum_{p=1}^{N_p} M_p \delta\left(\boldsymbol{x} - \boldsymbol{x}_p^t\right) \tag{1-4}$$

where δ is the Dirac delta function with dimension of the inverse of volume. The substitution of Eq. (1-4) into Eq. (1-3) converts the integrals to the sums of quantities evaluated at the material points, namely

$$\begin{aligned} &\sum_{p=1}^{N_p} M_p \left[\boldsymbol{w}\left(\boldsymbol{x}_{\boldsymbol{p}}^{\boldsymbol{t}},t\right)\cdot \boldsymbol{a}\left(\boldsymbol{x}_{\boldsymbol{p}}^{\boldsymbol{t}},t\right)\right] \\ &= \sum_{p=1}^{N_p} M_p \left[-\boldsymbol{s}^{\boldsymbol{s}}\left(\boldsymbol{x}_{\boldsymbol{p}}^{\boldsymbol{t}},t\right) : \nabla \boldsymbol{w}\big|_{\boldsymbol{x}_{\boldsymbol{p}}^{\boldsymbol{t}}} + \boldsymbol{w}\left(\boldsymbol{x}_{\boldsymbol{p}}^{\boldsymbol{t}},t\right)\cdot \boldsymbol{c}^{\boldsymbol{s}}\left(\boldsymbol{x}_{\boldsymbol{p}}^{\boldsymbol{t}},t\right)h^{-1} + \boldsymbol{w}\left(\boldsymbol{x}_{\boldsymbol{p}}^{\boldsymbol{t}},t\right)\cdot \boldsymbol{b}\left(\boldsymbol{x}_{\boldsymbol{p}}^{\boldsymbol{t}},t\right)\right] \end{aligned} \tag{1-5}$$

with h being the thickness of the boundary layer. As can be seen from Eq. (1-5), the interactions among different material points are reflected only through the gradient terms, and a suitable set of material points must be chosen to represent the boundary layer. In the MPM, a background computational mesh is required to calculate the gradient terms. To do so, suppose that a computational mesh is constructed of 2-node cells for one-dimensional problems, 4-node cells for two-dimensional problems, and 8-node cells for three-dimensional problems, respectively. These cells are then employed to define standard nodal basis functions, $N_i(\boldsymbol{x})$, associated with spatial nodes $\boldsymbol{x}_{\boldsymbol{i}}(t)$, $i = 1, 2, \ldots, N_n$, with N_n being the total number of mesh nodes. The nodal basis functions are assembled from conventional finite element shape functions. For instance, the shape functions for a 2-node cell take the forms of

$$N_1 = 1 - \xi \tag{1-6a}$$

$$N_2 = \xi \tag{1-6b}$$

where ξ is the natural coordinate of a material point in the cell along the x-direction. For two-dimensional problems, a 4-node cell is employed with the shape functions given by

$$N_1 = (1-\xi)(1-\eta) \tag{1-7a}$$

$$N_2 = \xi(1-\eta) \tag{1-7b}$$

$$N_3 = \xi\eta \tag{1-7c}$$

$$N_4 = (1-\xi)\eta \tag{1-7d}$$

in which ξ and η are the natural coordinates of a material point in the cell along the x- and y-direction, respectively. The coordinates of any material point in a cell can then be represented by

$$\boldsymbol{x}_p^t = \sum_{i=1}^{N_n} \boldsymbol{x}_i^t N_i\left(\boldsymbol{x}_p^t\right) \tag{1-8}$$

If the displacements of any material point in a cell are defined by the nodal displacements, $\boldsymbol{u}_i^t(t)$, it follows that

$$\boldsymbol{u}_p^t = \sum_{i=1}^{N_n} \boldsymbol{u}_i^t N_i\left(\boldsymbol{x}_p^t\right) \tag{1-9}$$

Since the same basis functions are used for both spatial coordinates and displacements, kinematic compatibility demands that the basis functions must advect with the material, as in the updated Lagrangian framework. In other words, the *material* time rates of the basis functions must be zero. Hence, it follows that the velocity and acceleration of any material point in a cell are represented by

$$\boldsymbol{v}_p^t = \sum_{i=1}^{N_n} \boldsymbol{v}_i^t N_i\left(\boldsymbol{x}_p^t\right) \tag{1-10}$$

and

$$\boldsymbol{a}_p^t = \sum_{i=1}^{N_n} \boldsymbol{a}_i^t N_i\left(\boldsymbol{x}_p^t\right) \tag{1-11}$$

with $\boldsymbol{v}_i^t$ and $\boldsymbol{a}_i^t$ being nodal velocities and accelerations, respectively. The test function has also this form,

$$\boldsymbol{w}_p^t = \sum_{i=1}^{N_n} \boldsymbol{w}_i^t N_i\left(\boldsymbol{x}_p^t\right) \tag{1-12}$$

The use of Eqs. (1-8)-(1-12) ensures that the associated vectors are continuous across the cell boundary. However, the gradients of these vectors are not continuous across the cell boundary due to the use of linear shape functions. Note that the variables evaluated at material points are related to the nodal values through the shape functions, as can be seen from Eqs. (1-8) - (1-12).

Substituting Eqs. (1-11) and (1-12) into Eq. (1-5) yields

$$\sum_{i=1}^{N_n} \boldsymbol{w}_i^t \cdot \sum_{i=1}^{N_n} m_{ij}^t \boldsymbol{a}_j^t$$

$$= -\sum_{i=1}^{N_n} \boldsymbol{w}_i^t \cdot \sum_{i=1}^{N_p} M_p \boldsymbol{s}_p^{s,t} \cdot \nabla N_i\big|_{\boldsymbol{x}_p^t} + \sum_{i=1}^{N_n} \boldsymbol{w}_i^t \cdot \boldsymbol{c}_i^t + \sum_{i=1}^{N_n} \boldsymbol{w}_i^t \cdot \boldsymbol{b}_i^t \tag{1-13}$$

at time t. In Eq. (1-13), the consistent mass matrix is given by

$$m_{ij}^t = \sum_{p=1}^{N_p} M_p N_i\left(\boldsymbol{x}_p^t\right) N_j\left(\boldsymbol{x}_p^t\right) \tag{1-14}$$

with corresponding lumped nodal masses

$$m_i^t = \sum_{i=1}^{N_p} M_p N_i\left(\boldsymbol{x}_p^t\right) \tag{1-15}$$

The discrete specific traction takes the form of

$$\boldsymbol{c}_i^t = \sum_{p=1}^{N_p} M_p \boldsymbol{c}_p^{s,t} h^{-1} N_i\left(\boldsymbol{x}_p^t\right) \tag{1-16}$$

with $\boldsymbol{c}_p^{s,t} = \boldsymbol{c}^s\left(\boldsymbol{x}_p^t, t\right)$, while the specific body force is discretized as

$$\boldsymbol{b}_i^t = \sum_{p=1}^{N_p} M_p \boldsymbol{b}_p^t N_i\left(\boldsymbol{x}_p^t\right) \tag{1-17a}$$

with $\boldsymbol{b}_p^t = \boldsymbol{b}\left(\boldsymbol{x}_p^t, t\right)$. Alternatively, if the vector $\boldsymbol{b}$ is a known function of position and time, as for gravity, then the nodal body force can be computed directly by

$$\boldsymbol{b}_i^t = \boldsymbol{b}\left(\boldsymbol{x}_p^t, t\right) m_i^t \tag{1-17b}$$

Since $\boldsymbol{w}_i^t$ are arbitrary except where the components of displacement are prescribed, Eq. (1-13) becomes

$$m_i^t \boldsymbol{a}_i^t = \left(\boldsymbol{f}_i^t\right)^{int} + \left(\boldsymbol{f}_i^t\right)^{ext} \tag{1-18}$$

for a lumped mass matrix, where the internal force vector is given by

$$\left(\boldsymbol{f}_i^t\right)^{int} = -\sum_{p=1}^{N_p} M_p \boldsymbol{s}_p^{s,t} \cdot \boldsymbol{G}_i\left(\boldsymbol{x}_p^t\right) \tag{1-19}$$

with $\boldsymbol{s}_p^{s,t} = \boldsymbol{s}^s\left(\boldsymbol{x}_p^t, t\right)$ and $\boldsymbol{G}_i\left(\boldsymbol{x}_p^t\right) = \nabla N_i\big|_{\boldsymbol{x}_p^t}$, and the external force vector is

$$\left(\boldsymbol{f}_i^t\right)^{ext} = \boldsymbol{c}_i^t + \boldsymbol{b}_i^t \tag{1-20}$$

As can be observed from Eqs. (1-15) - (1-17), and Eq. (19), the information is mapped from material points to the nodes of the cell containing these points, through the use of shape functions. If a material point is located in the center of a cell, the information from the particle would be equally mapped to the cell nodes, as can be found from the shape functions defined in Eqs. (1-6) and (1-7).

An explicit time integrator is used to solve Eq. (1-18) for the nodal accelerations, with the time step satisfying the stability condition, i.e., the critical time step being the ratio of the smallest cell size to the wave speed. The boundary conditions are enforced on the cell nodes, as discussed in more detail later. After the equations of motion are solved on the cell nodes, the new nodal values of velocity are then used to update the position of the material points. The strain increment for each material point is determined with the use of the gradient of the nodal basis function evaluated at the material point position. The corresponding stress increment can be found from the constitutive model. Any internal state variables can also be assigned to the material points and transported along with them. Once the material points have been completely updated, the computational mesh may be discarded, and a new mesh is defined, if desired, for the next time step.

As illustrated in Section 3 with a step-by-step solution scheme, the key feature of the MPM is the use of the same set of nodal basis functions for both the mapping from material points to cell nodes to solve Eq. (1-18), and the mapping from cell nodes to material points to update the material point information for the next time step.

2. Boundary and Shock Wave Treatments

ONE TENTATIVE METHOD

Since the equations of motion are solved on the cell nodes, it is natural to enforce both essential and natural boundary conditions on the nodes of the cells containing the

boundary particles. For essential boundary conditions, this treatment is consistent with the weak form of the governing equations because $\boldsymbol{w}_i^t$ are assumed to be zero on the essential boundary. For moving natural boundary conditions, we are tentatively proposing that the traction carried by the boundary particles should be mapped to the cell nodes according to Eq. (1-16), and the external force vector would then be formed based on Eq. (1-20). Since the continuum body is moving in an arbitrary computational mesh, all the boundary conditions are carried by the boundary particles. If only one boundary particle is located in a cell, the cell boundary becomes a part of the continuum boundary, and the cell size represents the thickness of boundary layer. If both boundary and interior particles of the continuum are located in a cell, this cell becomes a mixed one. However, the mixed cell is still treated as a boundary cell. In other words, the interior particles temporarily become boundary ones. To avoid numerical errors, therefore, small cells must be used to contain only boundary particles if possible, and the boundary conditions must be enforced in each time step. For instance, a quad-tree mesh refinement could be used near physical boundaries.

The essential boundary conditions considered here include no slip, prescribed tangential velocity and normal velocity, respectively. Because the shape functions are continuous, no-slip impact and penetration between bodies are handled automatically by the MPM without the need for any supplemental contact algorithm.

To produce a sharp shock wave front under impact, the viscous damping stress tensor, $\boldsymbol{q}_p^t$, is added to the material point stress tensor, $\boldsymbol{s}_p^t$ [York et al., 2000], based on the work by Wilkins [1980]. With $\boldsymbol{i}$ being the second order identity tensor, the viscous damping stress takes the form of

$$\boldsymbol{q}_p^t = \sqrt{c_{max}^2 g}\,\rho_p^t \lambda D_p^t \left[c_1 + \frac{c_2 \left| D_p^t \right|}{max \left| D_p^t \right|} \right] \boldsymbol{i} \tag{2-1}$$

where

$$D_p^t = \begin{cases} \nabla \cdot \boldsymbol{v}\big|_{\boldsymbol{x}_p^t} & \nabla \cdot \boldsymbol{v}\big|_{\boldsymbol{x}_p^t} < 0 \\ 0 & \nabla \cdot \boldsymbol{v}\big|_{\boldsymbol{x}_p^t} \geq 0 \end{cases} \tag{2-2}$$

In Eq. (2-1), c_{max} is the maximum sound speed, g is a geometric constant proportional to the mesh size, λ is an artificial bulk modulus, and c_1 and c_2 are constants. The variable D_p^t defined in Eq. (2-2) forces the viscous damping stress to be zero unless the material point is in compression. With different values of c_1 and c_2, a reasonable shock wave front can be obtained for given geometry, material properties and loading conditions.

ALTERNATIVE METHODS

The MPM has been herein shown to be a minor modification of the traditional finite element method. The classic nodal force and mass matrix integrals for the FEM grid are written in the usual FEM manner, but the MPM then discretizes these FEM integrals through the use of a Dirac delta function to approximate the density field.

Instead of invoking a Dirac delta density field, an alternative interpretation of the MPM is that the integrals (which are initially defined over the entire body) are broken up into a sum of integrals over the physical domains associated with the material particles. Of course, the actual shape of the particle domains is not monitored, so the sub-integrals cannot be computed exactly. For interior particle domains (i.e., particle domains that do not share a boundary with the true body boundary), information about the integrand is known only at the particles themselves; consequently, the best approximation of the integral is obtained by simple single-point integration. Using single point integration gives a result *at interior particles* that is identical to the result from using a Dirac delta density field. However, for boundary particles (i.e., particles whose physical boundary at least partly overlaps the body boundary), greater information is known about the integrand – one knows the value of fields at the particle and *also* at the particle's boundary. Consequently, the FEM integrals at boundary particles can be computed more accurately via a two-point integration scheme. With this approach, there is no need to introduce supplemental points lying on the body boundary itself. Instead, the interior particles that are abutted with the body boundary can be readily identified and endowed with additional geometrical information (i.e., a vector from the particle to the boundary location). Hence, rather than assuming uniform fields (i.e., single point integration), a linearly varying approximation to the fields can be constructed at boundary particles.

This approach would permit boundary conditions to readily propagate into the body's interior.

Again we reiterate that the MPM is really only a minor modification of traditional finite element methods where the finite element integrals are evaluated using an alternative set of *Lagrangian* integration points that are fully uncoupled from the choice of the finite element mesh. In every instance of MPM that we have seen to date, the mesh has been chosen to be rectangular for computational convenience. However, this does not have to be the case. The fact that the integration points (material particles) are Lagrangian makes them ideally suited for history-dependent constitutive models. The fact that the finite element mesh may be constructed with any desired topology makes the MPM appealing for large-deformation problems. Recognizing that the MPM is only a minor modification of traditional finite element methods, it makes good sense to develop an MPM code by retrofitting a mature production-quality FEM code. That way, all of the FEM infrastructure (graphics, data management, etc.) that took years to develop remains available. One such infrastructure already present in FEM codes is the ability to construct meshes that conform to the physical boundary of the body. So-called "arbitrary Lagrange-Eulerian codes" are able to use meshes that always move with the body boundary while allowing any level of remeshing on the interior of the body. This sort of capability suggests an ideal solution to the question of enforcing boundary conditions: by using a boundary conforming internally-refined ALE mesh, the boundary conditions could be imposed in the traditional FEM way! This benefit could very well outweigh the inconvenience of using traditional FEM meshes while retaining the advantage of permitting rezoning to avoid mesh tangling. This approach will be further explored in later work.

3. Solution Scheme

Based on the two-dimensional MPM code currently used at the University of Missouri-Columbia, a step-by-step solution scheme is given as follows, which consists of preprocessor, central processing unit and postprocessor.

Preprocessor

1. A continuum body is discretized into a set of material points with respect to the original configuration of the body. The number of material points depends on the number of the division of the body volume. Each material point carries its original material properties and has its own constitutive relation. The material points are followed throughout the deformation of the body, which provides a Lagrangian description of motion. An arbitrary computational grid can be used to find the natural coordinates of any material point, and the grid cell that contains the point. For the purpose of simplicity, however, a square grid with uniformly distributed cells is employed in the 2-D code, and the grid is fixed throughout the computation.

2. Initialize all the state variables (velocity, strain, stress, internal state variables, etc.) at the material points. Input the control parameters of the code.

Central Processing Unit

The detailed steps in each cycle are as follows:

1. <u>For each material point (particle), perform the mapping operation from particles to cell nodes</u>.

Map the mass from the particles to the nodes of the cell containing these particles,

$$m_i^t = \sum_{p=1}^{N_p} M_p N_i\left(\boldsymbol{x}_{\boldsymbol{p}}^{\boldsymbol{t}}\right) \tag{3-1}$$

where m_i^t is the mass at node i at time t, M_p the particle mass, N_i the shape function associated with node i, and $\boldsymbol{x}_{\boldsymbol{p}}^{\boldsymbol{t}}$ the location of the particle at t.

Map the momentum from the particles to the nodes of the cell containing these particles,

$$\left(m\boldsymbol{v}\right)_i^t = \sum_{p=1}^{N_p} \left(M\boldsymbol{v}\right)_p^t N_i\left(\boldsymbol{x}_{\boldsymbol{p}}^{t}\right) \tag{3-2}$$

where $\left(m\boldsymbol{v}\right)_i^t$ denotes the nodal momentum at node i at t, and $\left(M\boldsymbol{v}\right)_p^t$ the particle momentum at t.

Find the internal force vector at the grid nodes,

$$\left(\boldsymbol{f}_i^t\right)^{int} = -\sum_{p=1}^{N_p} \boldsymbol{G}_i\left(\boldsymbol{x}_p^t\right) \cdot \boldsymbol{s}_p^t \frac{M_p}{\rho_p^t} \tag{3-3}$$

in which $\boldsymbol{G}_i\left(\boldsymbol{x}_p^t\right)$ is the gradient of the shape function associated with node *i* evaluated at $\boldsymbol{x}_p^t$, $\boldsymbol{s}_p^t$ is the particle stress tensor at *t*, and ρ_p^t is the particle mass density at *t*.

2. Apply essential and natural boundary conditions to the grid nodes, and compute the nodal force vector,

$$\boldsymbol{f}_i^t = \left(\boldsymbol{f}_i^t\right)^{int} + \left(\boldsymbol{f}_i^t\right)^{ext} \tag{3-4}$$

where $\left(\boldsymbol{f}_i^t\right)^{ext}$ represents the external nodal force vector, as defined in Eq. (1-20).

3. Update the momenta at the grid nodes,

$$\left(m\boldsymbol{v}\right)_i^{t+\Delta t} = \left(m\boldsymbol{v}\right)_i^t + \boldsymbol{f}_i^t \Delta t \tag{3-5}$$

4. For each material particle, perform the mapping operation from the nodes of the cell containing the particle to the particle.

Map the nodal accelerations back to the particle,

$$\boldsymbol{a}_p^t = \sum_{i=1}^{N_n} \frac{\boldsymbol{f}_i^t}{m_i^t} N_i\left(\boldsymbol{x}_p^t\right) \tag{3-6}$$

Map the current nodal velocities back to the particle,

$$\bar{\boldsymbol{v}}_p^{t+\Delta t} = \sum_{i=1}^{N_n} \frac{\left(m\boldsymbol{v}\right)_i^{t+\Delta t}}{m_i^t} N_i\left(\boldsymbol{x}_p^t\right) \tag{3-7}$$

Compute the current particle velocity for strain calculations,

$$\boldsymbol{v}_p^{t+\Delta t} = \boldsymbol{v}_p^t + \boldsymbol{a}_p^t \Delta t \tag{3-8}$$

Compute the current particle position,

$$\boldsymbol{x}_p^{t+\Delta t} = \boldsymbol{x}_p^t + \bar{\boldsymbol{v}}_p^{t+\Delta t} \Delta t \tag{3-9}$$

Equation (3-9) represents a backward integration.

Compute the particle displacement vector,

$$\boldsymbol{u}_p^{t+\Delta t} = \boldsymbol{x}_p^{t+\Delta t} - \boldsymbol{x}_p^{0} \tag{3-10}$$

As can be seen from Eqs. (3-7) and (3-9), nodal shape functions are used to map the nodal velocity continuously to the interior of the cell so that the position of the particles are updated by moving them in a single-valued, continuous velocity field. Because the velocity $\bar{\boldsymbol{v}}_p^{t+\Delta t}$ instead of the velocity $\boldsymbol{v}_p^{t+\Delta t}$ is used to update the particle position to reduce the potential numerical error, interpenetration between material bodies is precluded in numerical solutions. This unique feature of the MPM allows simulations of impact and penetration problems without the need for a special contact algorithm.

5. Map the updated particle momenta back to the nodes of the cell containing these particles,

$$(m\boldsymbol{v})_i^{t+\Delta t} = \sum_{p=1}^{N_p} (M\boldsymbol{v})_p^{t+\Delta t} N_i\left(\boldsymbol{x}_p^t\right) \tag{3-11}$$

6. Find the updated nodal velocities,

$$\boldsymbol{v}_i^{t+\Delta t} = \frac{(m\boldsymbol{v})_i^{t+\Delta t}}{m_i^t} \tag{3-12}$$

7. Apply the essential boundary conditions to the grid nodes of the cells containing the boundary particles. For the essential boundary conditions, this treatment is consistent with the weak form of the governing equations because $\boldsymbol{w}_i^t$ are assumed to be zero on the essential boundary

8. If needed for a constitutive model, find the current gradient of particle velocity

$$\boldsymbol{L}_p^{t+\Delta t} = \sum_{i=1}^{N_n} \boldsymbol{v}_i^{t+\Delta t} \boldsymbol{G}_i\left(\boldsymbol{x}_p^t\right) \tag{3-13a}$$

the particle strain increment

$$\Delta \boldsymbol{e}_p = \left(sym \boldsymbol{L}_p^{t+\Delta t}\right)\Delta t \tag{3-13b}$$

and the updated deformation gradient tensor

$$\boldsymbol{F}_p^{t+\Delta t} = \sum_{i=1}^{N_n} \boldsymbol{x}_p^{t+\Delta t} \boldsymbol{G}_i\left(\boldsymbol{x}_p^t\right) \cdot \boldsymbol{F}_p^t \tag{3-13c}$$

9. Find the stress increment from the constitutive model for the given strain increment, and update the particle stress tensor,

$$\boldsymbol{s}_p^{t+\Delta t} = \boldsymbol{s}_p^t + \Delta \boldsymbol{s} \tag{3-14}$$

10. Identify which grid cell each particle belongs to, and update the natural coordinates of the particle. This is the convective phase for the next time increment.

11. Go to Step 1 for the next time increment, if the required termination time has not been reached.

As can be found from Eqs. (3.6), (3.7) and (3.12), the numerical solution process would be broken if m_i^t is close to zero, which happens when no particles exist within the support domain of N_i. If m_i^t is less than a small number set by machine precision, these equations are not calculated in the code.

4. Verification and Demonstration

To test the completeness of the solution scheme and demonstrate the features of the MPM, a one-dimensional MPM code is developed here, without considering the viscous damping stress, to solve one-dimensional wave and impact problems. The simplicity of 1-D problems makes it possible to provide a deeper insight into the unique features of the MPM than 2-D and 3-D problems.

Consider an elastic bar with length $L = 1$, Young's modulus $E = 10000$, Poisson's ratio $\nu = 0$, and mass density $\rho = 1$ so that the wave speed is $C = \sqrt{E/\rho} = 100$. In the first test problem, a tensile step force $f = 1$ is applied to the bar's right end, with its left end being fixed. Here, we have intentionally defined a problem involving only infinitesimal displacements so that the effects of particle convection and moving boundary can be avoided, which permits a fair comparison between the MPM and FEM solutions. In the MPM simulation, the number of cells is the same as that of particles; in other words, one particle per cell is used. As shown in Figs. 1-2, the stress wave profiles are improved if the number of particles is increased from 10 to 500, which is similar to the finite element solutions with single-point Gauss integration. Both essential and natural boundary conditions are enforced at the boundary cell nodes, while the stress is evaluated at the particles. To investigate whether the code will separate particles when the tensile waves meet in the center, Figs. 3a and 3b demonstrate the wave propagation along the same elastic bar, but the boundary condition becomes that both ends are subjected to a step force $f = 1$. By replacing the tensile step force with a compressive rectangular impulse of magnitude 1 and duration L/C, applied at both ends of the bar, Figs. 4a and 4b illustrate the wave propagation along the elastic bar. Again, the numerical solutions are similar to the finite element solutions. As can be seen from Figs. 5 and 6, no separation occurs in both tension and compression. The reason is that the existence of at least one particle per cell causes the material to be treated as contiguous and coherent, namely, no separation.

Now consider the impact between two elastic bars of equal length L = 0.5, with the same material properties as before. The motion of the bars and the corresponding stress wave profiles are shown in Figs. 7-10. As can be seen, two bars start to separate

from each other when the reflected tensile waves cancel the compressive waves and reach the middle point. To test whether a cell without a particle represents a space, elastic wave propagation in two bars separated by an empty cell is examined in Figs. 11-12. The results appear to be reasonable. To investigate the impact between two elastoplastic bars, the motion of the bars and the corresponding stress profiles are given in Figs. 13-16, for a linear strain-hardening model with elasto-plastic tangent modulus being a quarter of Young's modulus, and in Figs. 17-20, for an elastic-perfect-plastic model. These figures demonstrate the capability of the MPM to simulate impact and wave responses.

To further demonstrate the contact/impact scheme of the MPM, consider the impact between two separate elastic bars of unit area with an initial velocity V_0. Recall that each nodal value of any field is influenced only by those particles within the support domain of the node. Therefore, the velocity gradient is nonzero only if the particles within the support domain of the node have different velocities. While the left and right bars are freely translating in the space, with a constant speed, we know that the velocity gradient in each bar must be zero based on the physics. This physical property is preserved in the MPM because the velocity assigned to the boundary node is determined by the particle in the support domain of that node. As can be observed from Eqs. (3.1), (3.2) and (3.12),, the boundary nodal velocity is equal to the boundary particle velocity, and the boundary particle therefore experiences no velocity gradient, as long as the nodal force vector is zero. This is the case for a bar moving in the space with a constant velocity the nodal momenta will not change with time as shown in Eq. (3.5). A zero velocity gradient will persist until the support domain of the boundary node contains particles with different velocities. Consequently, the two bars will not interact with each other until the boundary particle of each bar is within the support domain of a single node.

Just before impact as shown in Fig. 0-1, the strain increment of particle $\bar{3}$ and $\bar{4}$, can be calculated, from the shape functions defined in Eq. (1-6), to be

$$\Delta e_{\bar{3}} = \frac{0 - v_3}{h_c}\Delta t = -\frac{v_3}{h_c}\Delta t < 0 \tag{4-1}$$

and

$$\Delta e_{\bar{4}} = \frac{v_5 - 0}{h_c}\Delta t = \frac{v_5 - 0}{h_c}\Delta t < 0 \tag{4-2}$$

respectively, because of $v_3 > 0$, $v_4 = 0$ and $v_5 < 0$. In Eqs. (4-1) and (4-2), h_c represents the cell size.

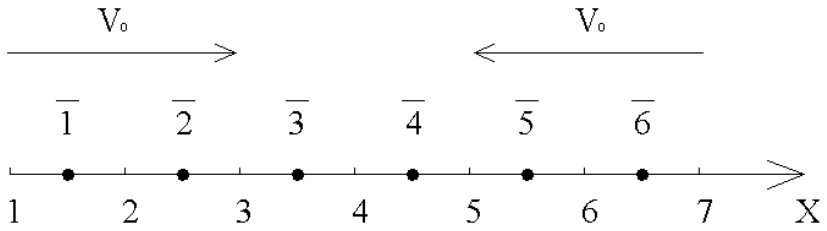

Figure 0-1

The corresponding stress increments are given by $\Delta s_{\bar{3}} = E\Delta e_{\bar{3}}$ and $\Delta s_{\bar{4}} = E\Delta e_{\bar{4}}$. The stress distribution just after impact is shown in Fig. 0-2.

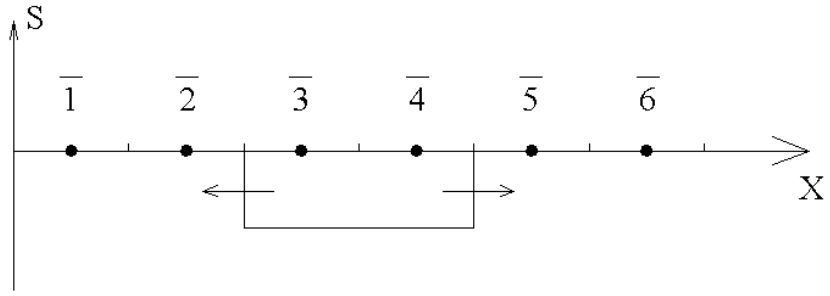

Figure 0-2

In the restitution phase, the reflected tensile wave cancels the compressive wave. Just before separation, the stress distribution is depicted in Fig. 0-3.

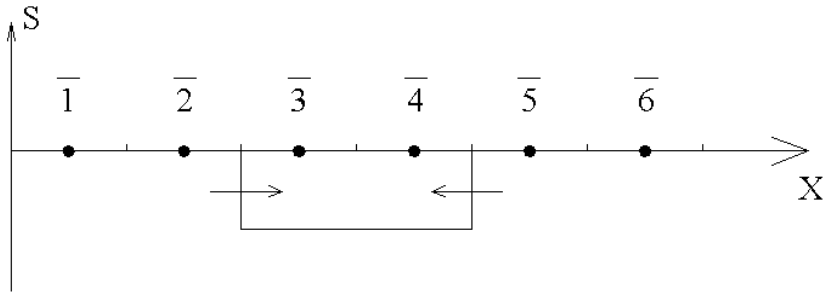

Figure 0-3

Just before and after impact, the force mapped from particle $\bar{3}$ to node *3* is given by

$$f_3 = -\left(-\frac{1}{h_c}\right)s_{\bar{3}} = \frac{s_{\bar{3}}}{h_c} < 0 \tag{4-3}$$

as can be found from Figs. 0-2 and 0-3. The force mapped from particle $\bar{4}$ to node *5* is given by

$$f_5 = -\left(\frac{1}{h_c}\right)s_{\bar{4}} = -\frac{s_{\bar{4}}}{h_c} > 0 \tag{4-4}$$

At node *4*, $f_4 = 0$ because the forces mapped from particle $\bar{3}$ and $\bar{4}$ cancel each other. Hence, particles $\bar{3}$ and $\bar{4}$ will move away from each other once just before impact, and again just after impact. As a result, two bars separate from each other.

The above case is in contrast to the case where a bar is subjected to compressive forces at both ends. As can be seen from Figs. 4 and 6 that are discussed before, the center particles will move toward each other, when two compressive waves meet at the center, in the same amount as they move away from each other when reflected tensile waves cancel the compressive waves at the center. At $t = 1.5L/C$, the center particles move back to its original positions. Hence, the single bar will not be separated at the center in the MPM simulation.

Now consider a single elastic bar of unit area under tensile loading at both ends, as shown in Fig. 0-4.

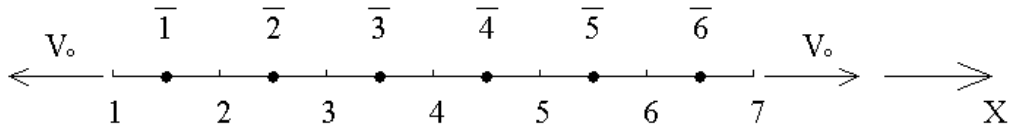

Figure 0-4

Just after two tensile waves meet at the middle point of the bar, the stress distribution is demonstrated in Fig. 0-5.

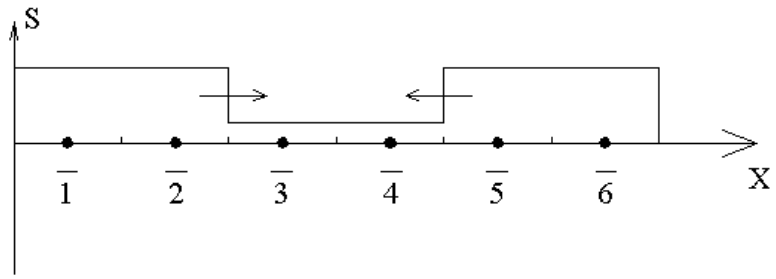

Figure 0-5

Since the magnitude of the reaction from particle $\bar{5}$ to node 5, $\left|f_{\bar{5}-5}\right|$, is larger than that from particle $\bar{4}$ to node 5, $\left|f_{\bar{4}-5}\right|$, particle $\bar{4}$ moves toward node 5. Similarly, particle $\bar{3}$ moves toward node 3.

After the stress wave is doubled at the middle point of the bar, the stress distribution is shown in Fig. 0-6.

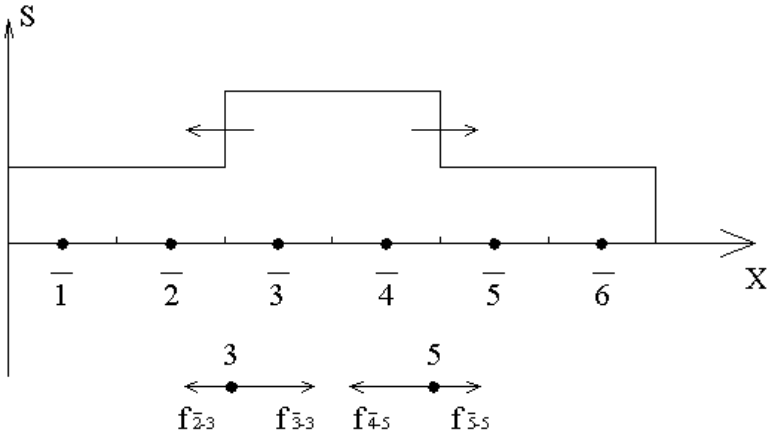

Figure 0-6

Now the magnitude of the reaction from particle $\bar{5}$ to node 5, $\left|f_{\bar{5}-5}\right|$, is less than that from particle $\bar{4}$ to node 5, $\left|f_{\bar{4}-5}\right|$, so that particle $\bar{4}$ moves toward node 4. Similarly, particle $\bar{3}$ moves toward node 4. Hence, both particles $\bar{3}$ and $\bar{4}$ would move toward each other. In other words, the bar would not be separated at the center.

As can be seen from the above qualitative analysis, the MPM can simulate the contact/impact phenomena based on the physics involved, without invoking master/slave nodes as required in the conventional mesh-based methods

5. Comparison of the MPM with Other Meshless Methods

As indicated by Belytschko et al. [1996], the meshless (meshfree) methods are uniquely suitable for those problems, for which the conventional mesh-based methods are handicapped, such as localized large deformations, propagation of cracks and separation of continuum. In fact, the key difference among different spatial discretization methods is how the gradient and divergence terms are calculated. Because the meshless methods do not use a rigid mesh connectivity as compared with the FEM, FDM and BEM, the interpolation in the moving domain of influence is the common feature of the meshless methods. Although a background mesh is used to calculate the gradient and divergence terms, the MPM is still based on the interpolation in the moving domain of influence, namely, the spatial discretization is continuously adjusted as a body deforms. Thus, the MPM can be considered as one of the meshless methods. To our knowledge, all existing meshless methods employ some sort of moving domain of influence to find the gradient and divergence terms. Hence, the word "meshless" should be interpreted as meaning that a rigid mesh connectivity is not used in spatial discretization.

The MPM is an extension to solid mechanics problems of a hydrodynamics code called FLIP which, in turn, evolved from the Particle-in-Cell Method for fluid flow. The motivation of the development was to simulate those challenging problems in solid mechanics, such as impact/contact, penetration and perforation, with history-dependent internal state variables. As can be found from the theoretical framework and solution scheme discussed above, the MPM combines the advantages of Eulerian and Lagrangian descriptions of the material while avoiding the shortcomings of each. In comparison with the other meshless methods, the MPM appears to be less complex with a cost factor of at most twice that associated with the use of corresponding finite elements. Due to the mapping from material points to cell nodes and the mapping from cell nodes to material points involved in each time step, the MPM can simulate localized large deformations without mesh tangling. The use of the same set of continuous shape functions in both

mappings results in a natural no-slip contact/impact scheme so that no inter-penetration would occur. However, special treatments must be invoked if decohesion and the moving surface of discontinuity occur in the deformation process, which is under current research.

Other meshfree methods, such as the Moving Least Square (MLS) approximation in the Element-Free Galerkin method or the Reproducing Kernel (RK) approximation [Belytschko et al., 1996; Chen et al., 1998; Liu et al., 1997; among others], were developed specifically for localization and crack propagation problems. However, the routine use of these methods for a wide range of applications appears not to be feasible, because of the complexity involved in their current forms. The computational cost of explicit forms of the Element-Free Galerkin method exceeds that of low-order finite elements by a factor of about 4. If penetration and perforation need be simulated, master/slave type of constraints must be imposed on the spatial discretization procedure. On the other hand, an alternative approach, which is less complex and appears promising for penetration and perforation, is that based on smooth particle hydrodynamics [Johnson et al., 1996; Randles and Libersky, 1996]. However, prevention of inter-penetration and instability under tensile stresses requires special treatments with this approach.

With a focus on arbitrary domains, the H_p cloud method has been recently developed by employing only a scattered set of nodes to build approximate solutions to general boundary-value problems [Duarte and Oden, 1995]. This method exhibits a very high rate of convergence and has a greater flexibility than traditional *hp* finite element methods. However, it has not been applied to penetration and perforation problems.

Based on the literature survey, it appears that the MPM is particularly well-suited to penetration and perforation problems, and is easily implemented, as compared with other meshless methods.

6. Conclusion and Future Work

The theory and algorithm for the MPM have been documented, based on which the treatments of boundary conditions and shock wave problems have been discussed. To test the completeness of the numerical algorithm and to demonstrate the features of the MPM, a one-dimensional MPM code has been programmed to solve one-dimensional

wave and impact problems, with both linear elasticity and elastoplasticity models. The contact/impact scheme has been qualitatively illustrated via bar problems. The advantages and disadvantages of the MPM have been investigated as compared with competing meshfree methods.

Based on the current work, it appears that different meshfree methods have a common feature, viz., the use of a moving domain of influence. In other words, the spatial discretization is continuously adjusted as a body deforms. With the use of different approaches to calculate gradient and divergence terms, different meshfree methods have demonstrated the robustness and potential in different types of problems. Future research will aim at taking advantages of different spatial discretization methods, including both mesh-based and meshfree ones, to better simulate those complex physical problems such as impact/contact, localization, crack propagation, penetration, perforation, fragmentation, and interactions among different material phases, in a unified computational framework.

7. References

Belytschko, T., Krongauz, Y., Organ, D., Fleming, M., and Krysl, P. (1996), "Meshless Methods: An Overview and Recent Developments," *Computer Methods in Applied Mechanics and Engineering*, Vol. 139, pp. 3-48.

Chen, J.S., Pan, C., Roque, C., Wang, H.P. (1998), "A Lagrangian Reproducing Kernel Particle Method for Metal Forming Analysis," *Computational Mechanics*, Vol. 22, pp. 289-307.

Duarte, C.A., and Oden, J.T. (1995), "H_p Clouds – A Meshless Method to Solve Boundary-Value Problems," TICAM Report 95-05.

Harlow, F.H. (1964), "The Particle-in-Cell Computing Method for Fluid Dynamics in Fundamental Methods in Hydrodynamics," *Experimental Arithmetic, High-Speed Computations and Mathematics*, Edited by B. Alder, S. Fernbach and M. Rotenberg, Academic Press, pp. 319-345.

Johnson, G.R., Stryk, R.A., and Beissel, S.R. (1996), "SPH for High Velocity Impact Computations," *Computer Methods in Applied Mechanics and Engineering*, Vol. 139, pp. 347-374.

Liu, W.K., Li, S., Belytschko, T. (1997), "Moving Least Square Kernel Galerkin Method, Parat I. Methodology and Convergence," *Computer Methods in Applied Mechanics and Engineering*, Vol. 143, pp. 422-433.

Randles, P.W., and Libersky, L.D. (1996), "Smoothed Particle Hydrodynamics: Some Recent Improvements and Applications," *Computer Methods in Applied Mechanics and Engineering*, Vol. 139, pp. 375-408.

Sulsky, D., Chen, Z., and Schreyer, H.L. (1994), "A Particle Method for History-Dependent Materials," *Computer Methods in Applied Mechanics and Engineering*, Vol. 118, pp. 179-196.

Sulsky, D., Zhou, S.J., and Schreyer, H.L. (1995), "Application of a Particle-in-Cell Method to Solid Mechanics," *Computer Physics Communications*, Vol. 87, pp. 236-252.

Sulsky, D., and Schreyer, H.L. (1996), "Axisymmetric Form of the Material Point Method with Applications to Upsetting and Taylor Impact Problems," *Computer Methods in Applied Mechanics and Engineering*, Vol. 139, pp. 409-429.

References (cont'd)

Wilkins, M.L. (1980), "Use of Artificial Viscosity in Multidimensional Fluid Dynamic Calculations," *Journal of Computational Physics*, Vol. 36, pp. 281-303.

York, A.R. II, Sulsky, D., and Schreyer, H.L. (2001), "Fluid-Membrane Interaction Based on the Material Point Method," accepted for publication in *International Journal for Numerical Methods in Engineering*.

Figures

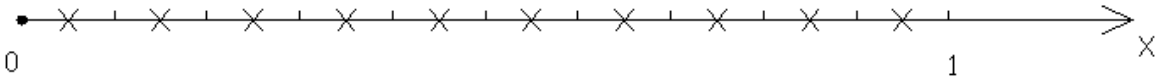

Figure 1. An elastic bar with its left end fixed and right end subjected to a tensile step force (Np=10). Here, hash marks indicate cell boundaries, and X's mark the (initially cell-centered) particle locations.

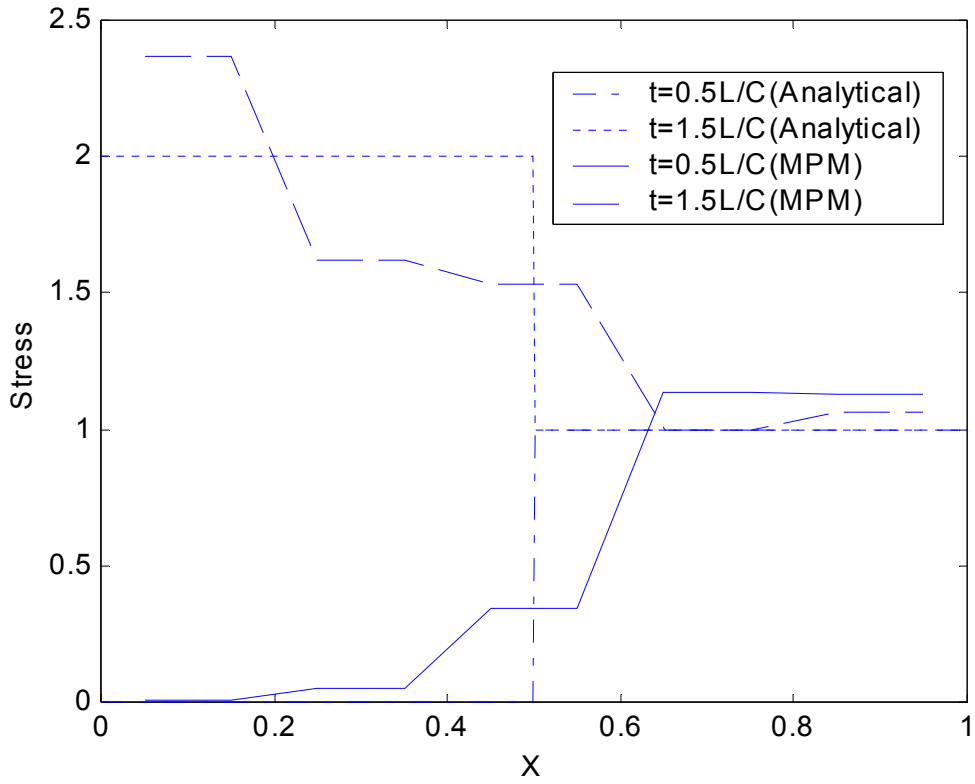

Figure 2a. Stress wave propagation along the bar (Np=10).

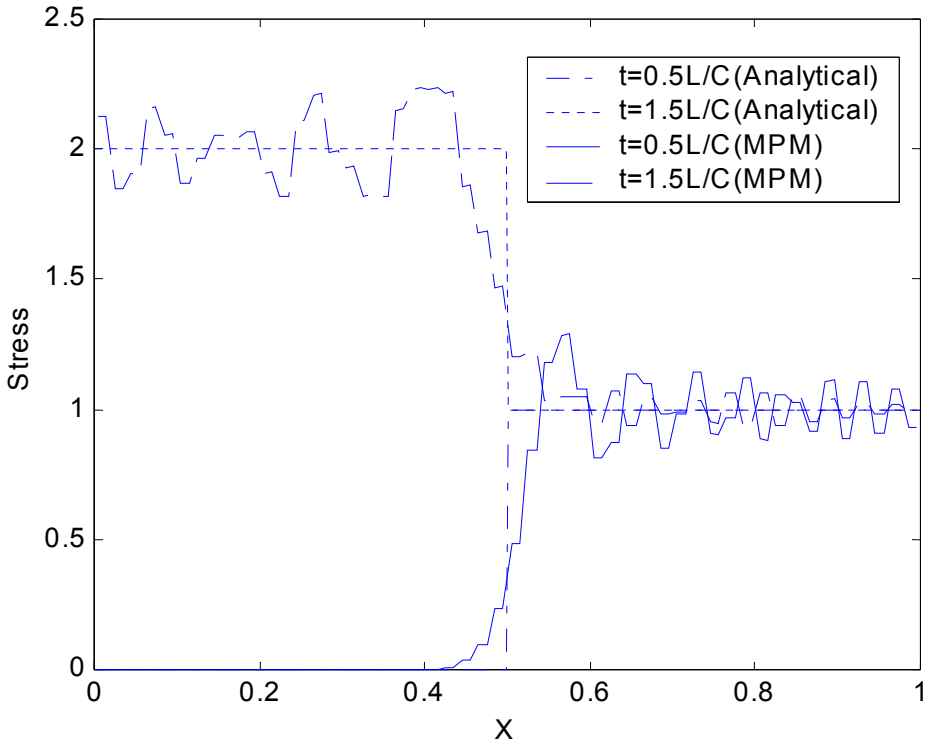

Figure 2b. Stress wave propagation along the bar (Np=100).

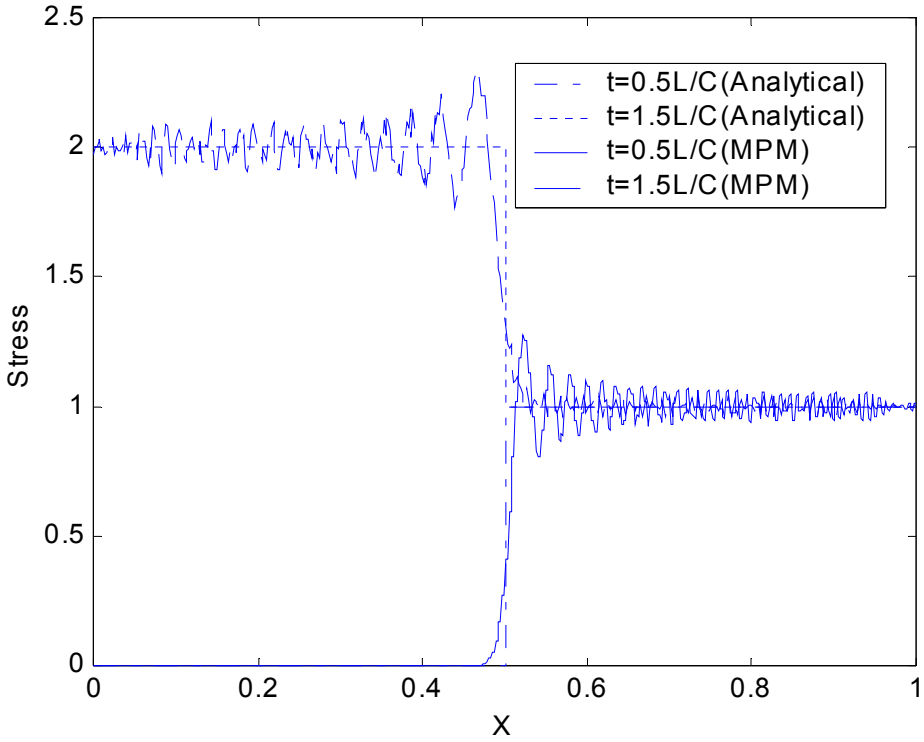

Figure 2c. Stress wave propagation along the bar (Np=500).

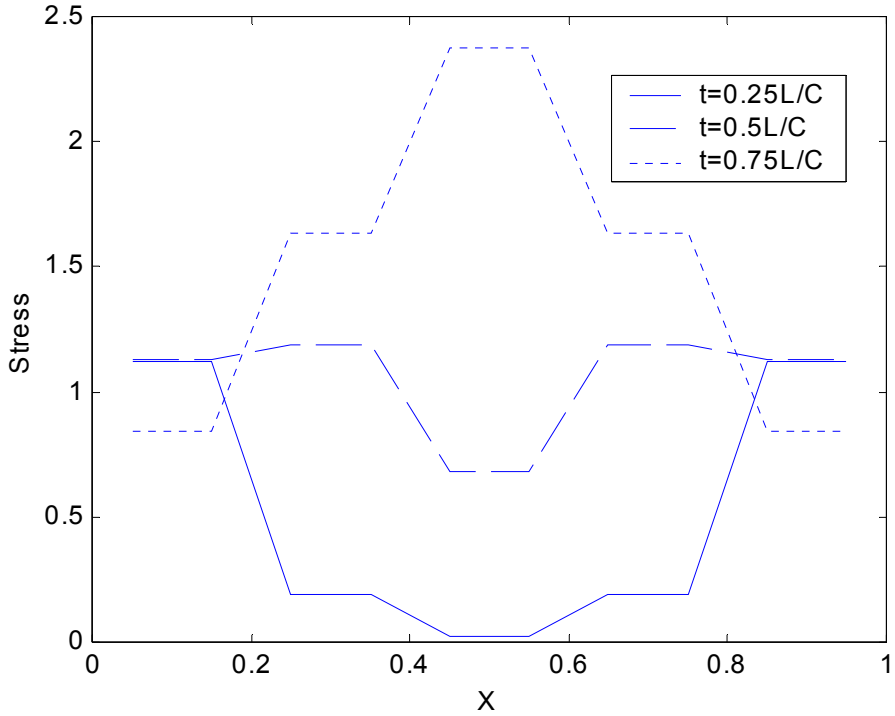

Figure 3a. Elastic stress wave propagation along a bar with both ends subjected to a tensile step force (Np=10).

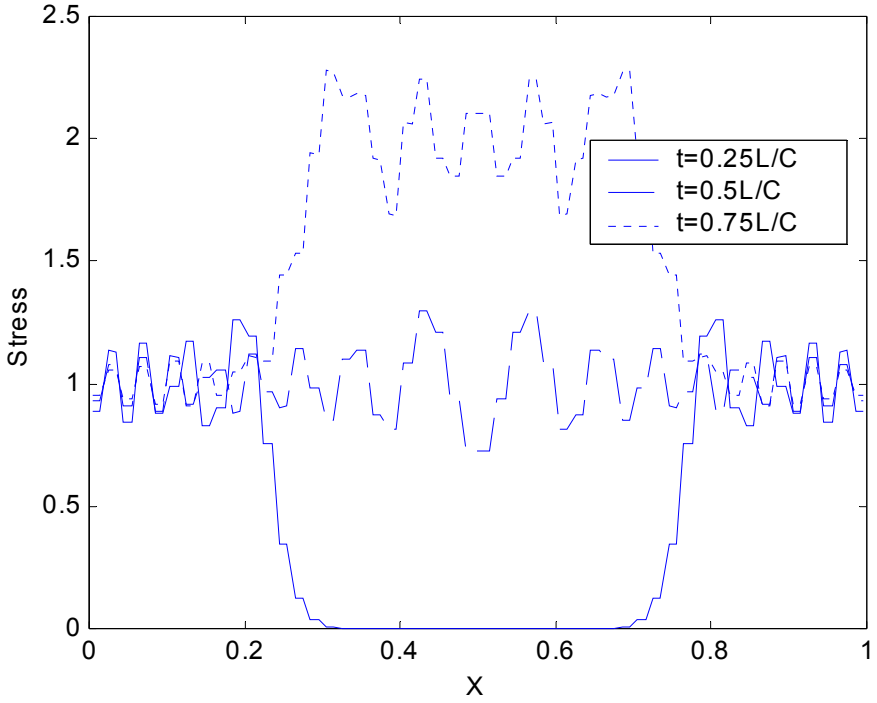

Figure 3b. Elastic stress wave propagation along a bar with both ends subjected to a tensile step force (Np=100).

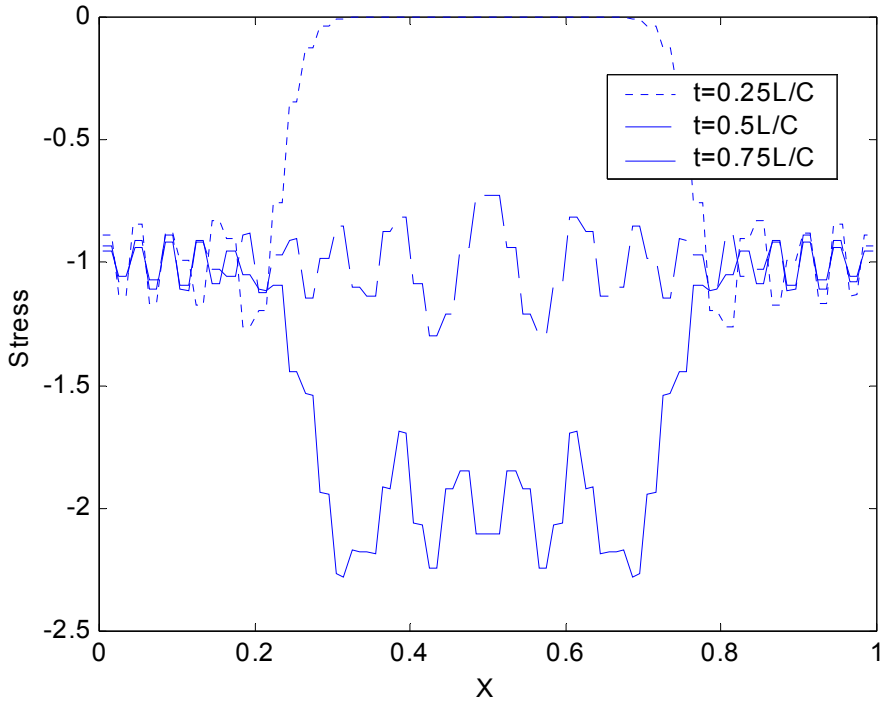

Figure 4a. Elastic stress wave propagation along a bar with both ends subjected to a compressive rectangular impulse force (Np=100).

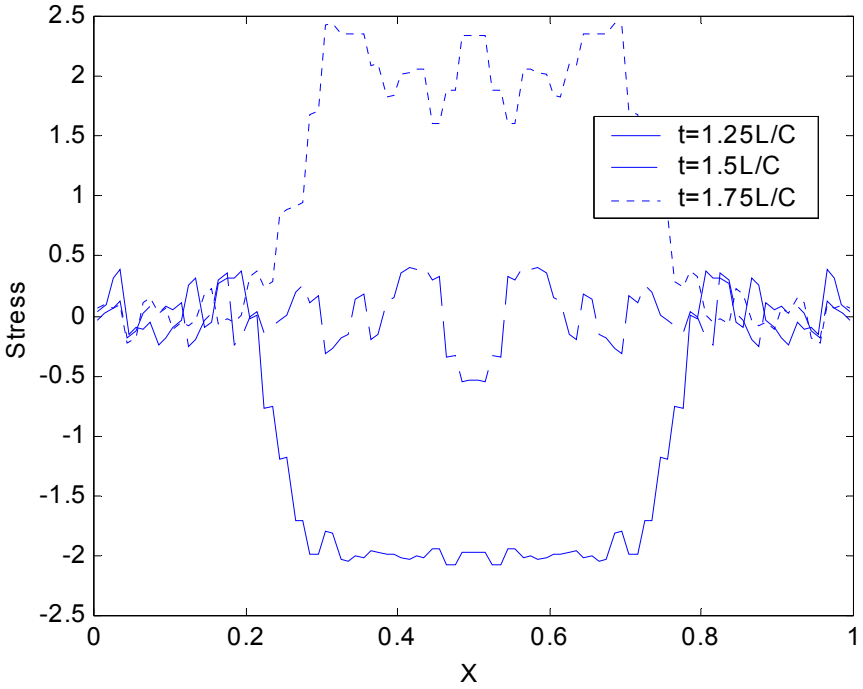

Figure 4b. Elastic stress wave propagation along a bar with both ends subjected to a compressive rectangular impulse force (Np=100).

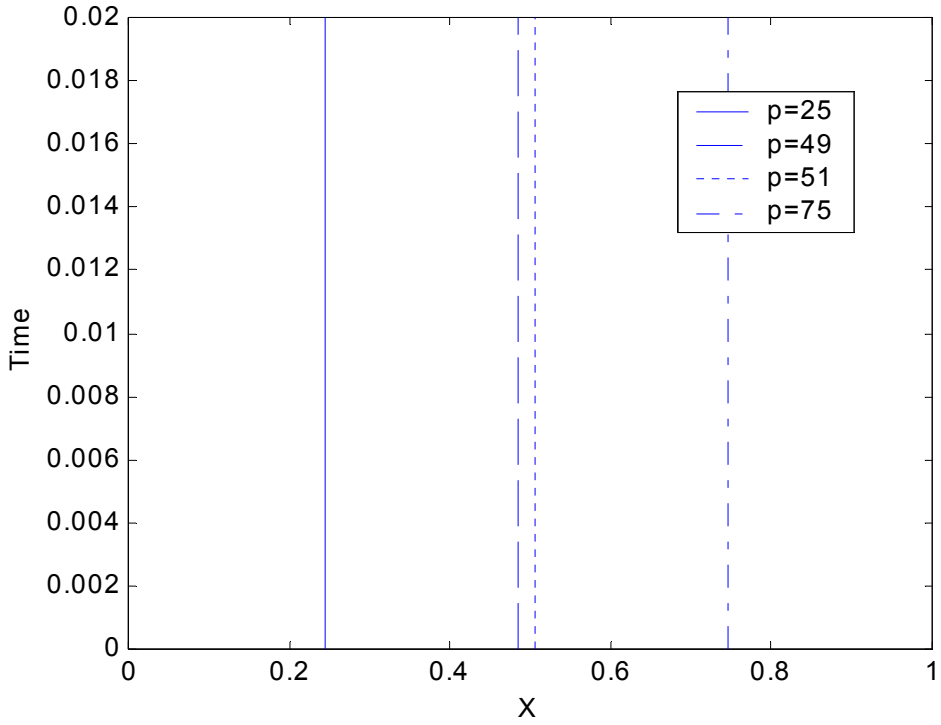

Figure 5. The motion of selected particles along a bar with both ends subjected to a tensile step force (Np=100).

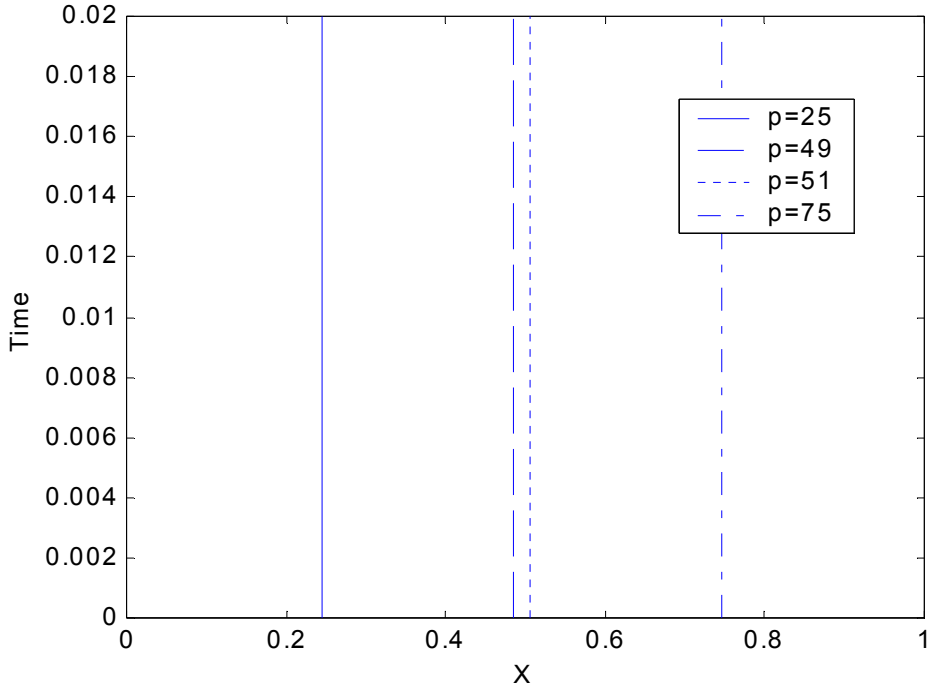

Figure 6. The motion of selected particles along a bar with both ends subjected to a compressive rectangular impulse force (Np=100).

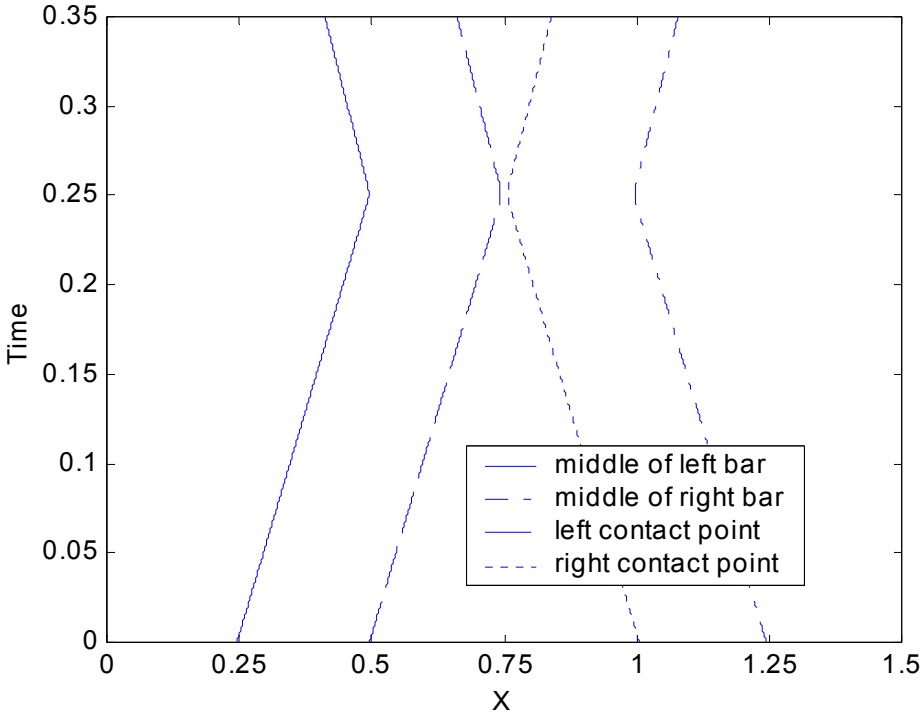

Figure 7. The impact between two elastic bars (Np=50 for each bar), the distance between which is 0.5 at t=0. The bars remain in contact for a time of 2L/C.

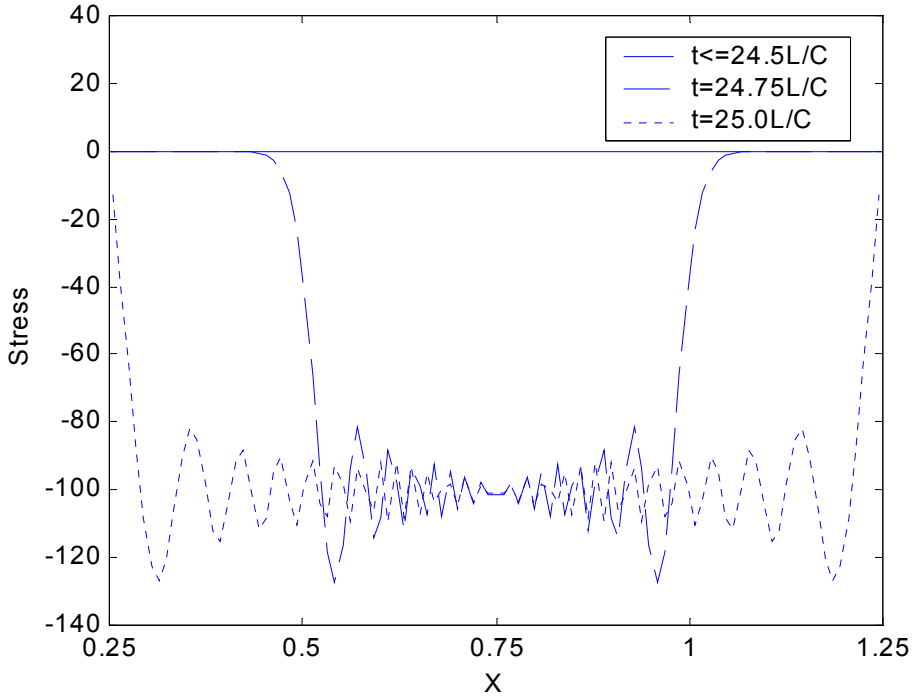

Figure 8. The changes in the stress profile corresponding to Figure 7.

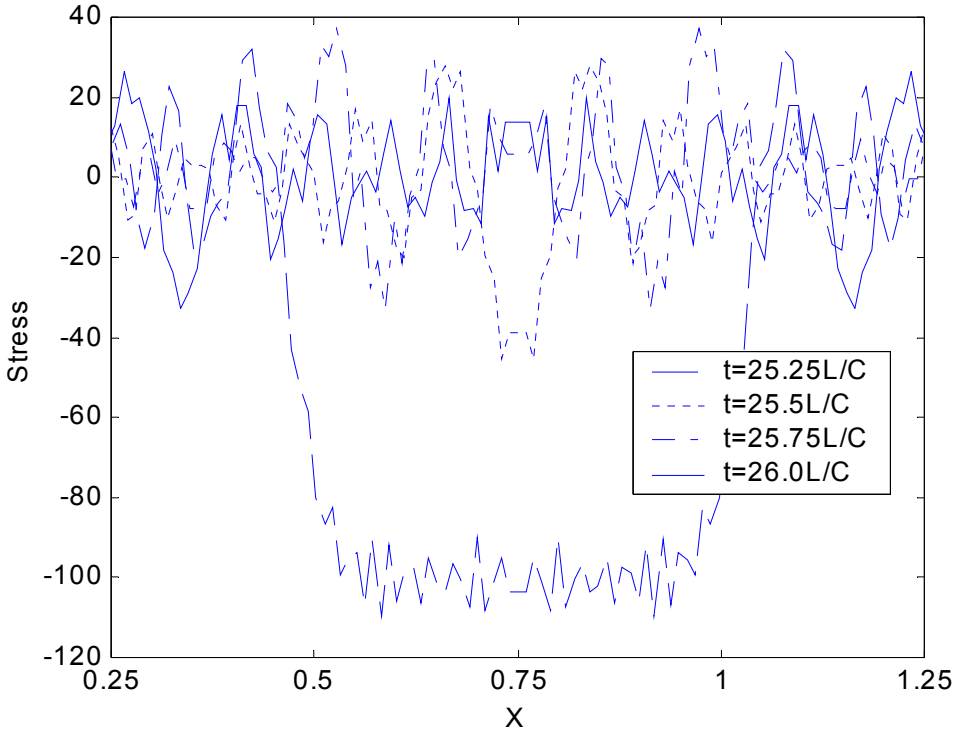

Figure 9. The continuation of Figure 8.

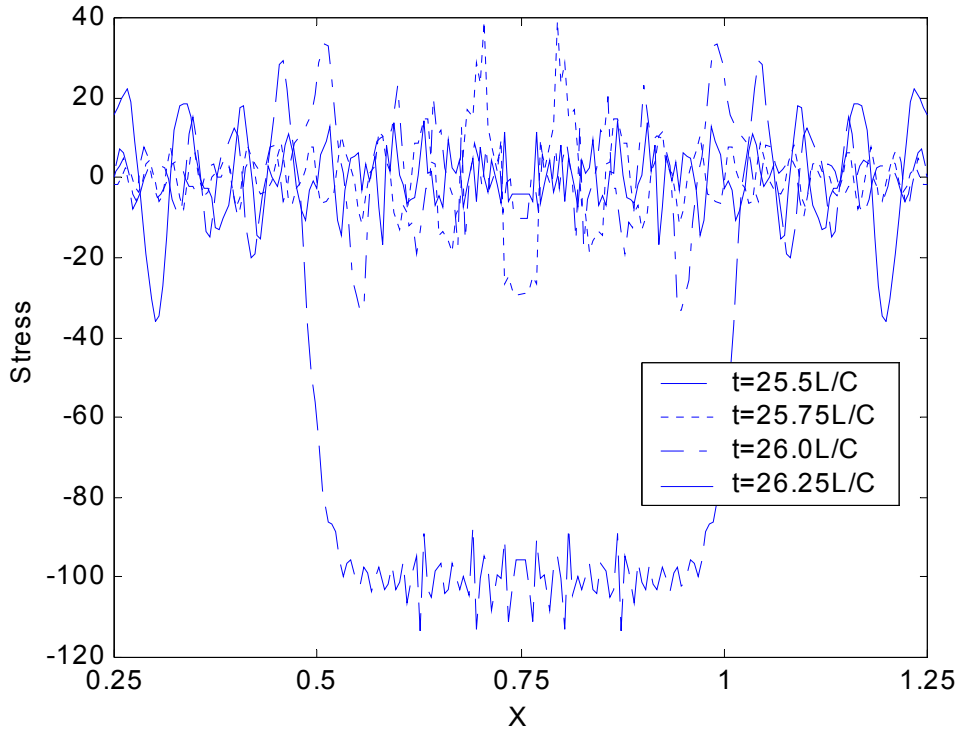

Figure 10. The changes in the stress profile corresponding to Figure 9, with Np=100 for each bar.

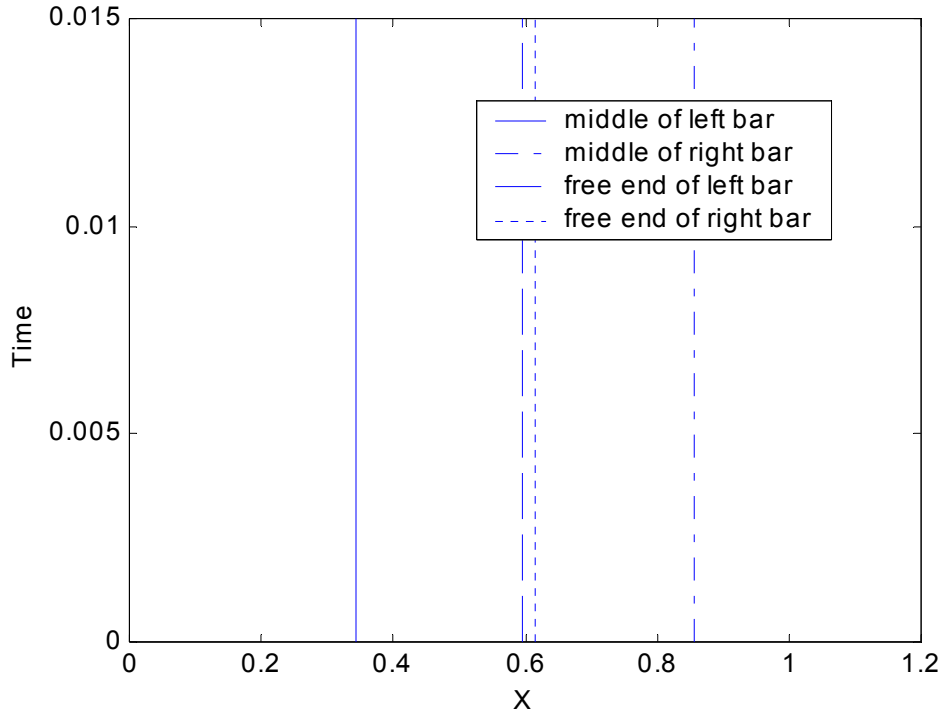

Figure 11. Elastic wave propagation in two separated bars (Np=50 for each bar), with the left end of the left bar and the right end of the right bar being subjected to a tensile step force, respectively.

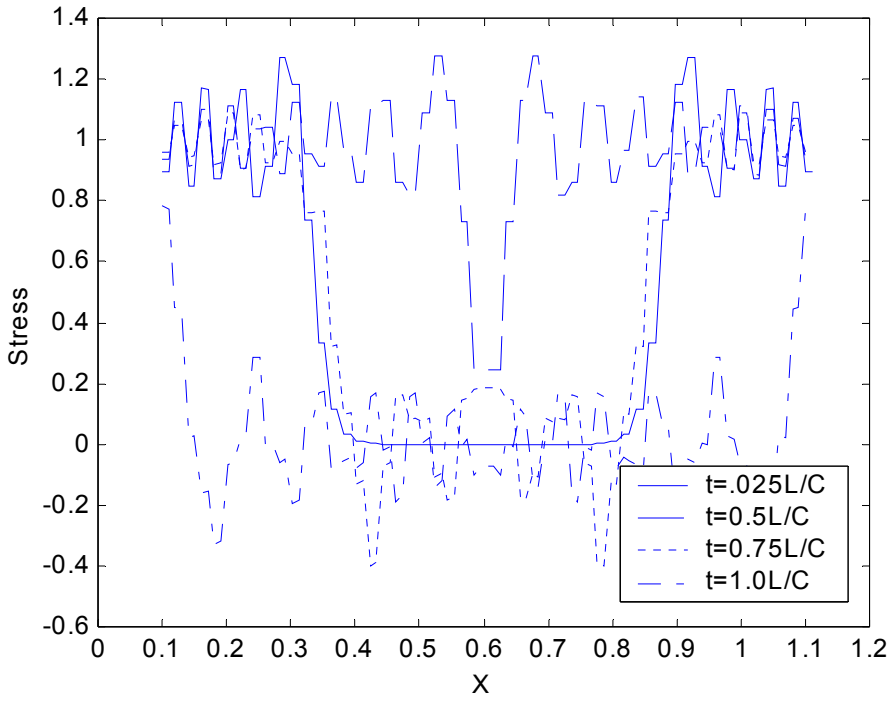

Figure 12. The stress profile corresponding to Figure 11.

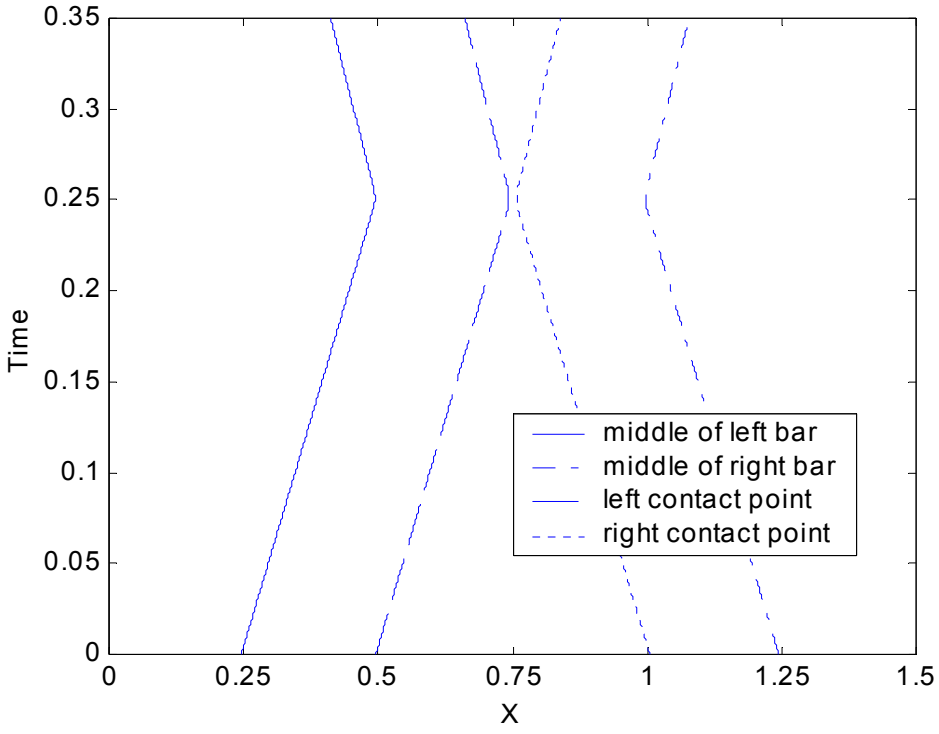

Figure 13. The impact between two elastic-hardening bars (Np=50 for each bar), the distance between which is 0.5 at t=0.

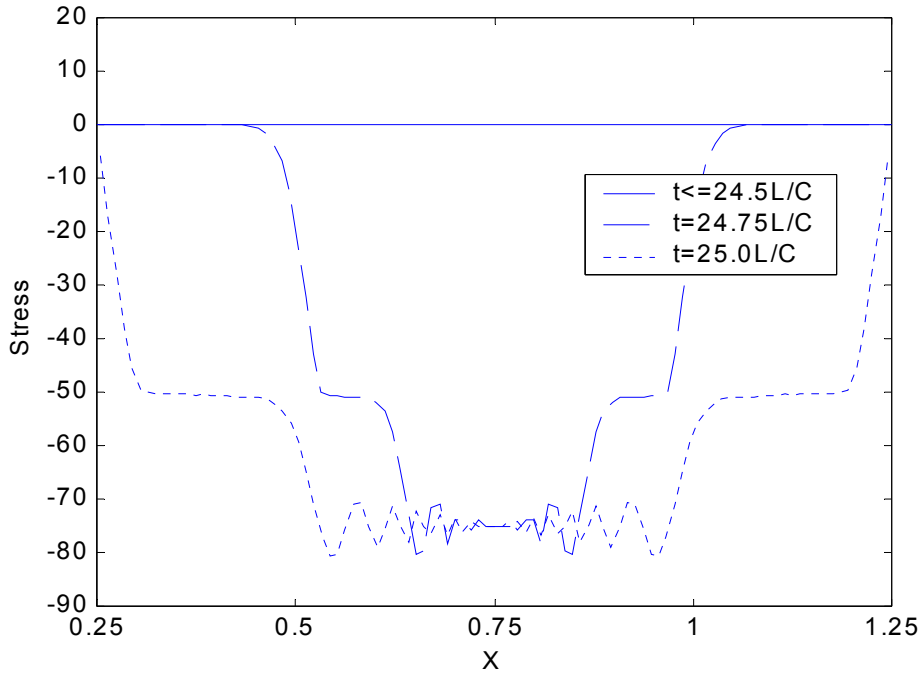

Figure 14. The changes in the stress profile corresponding to Figure 13.

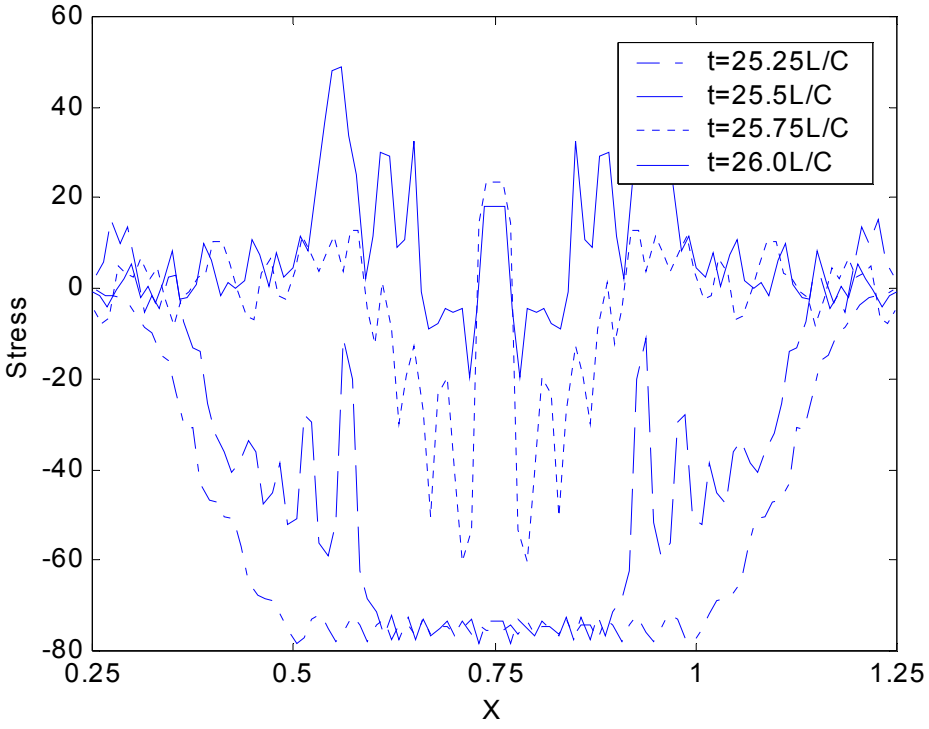

Figure 15. The continuation of Figure 14.

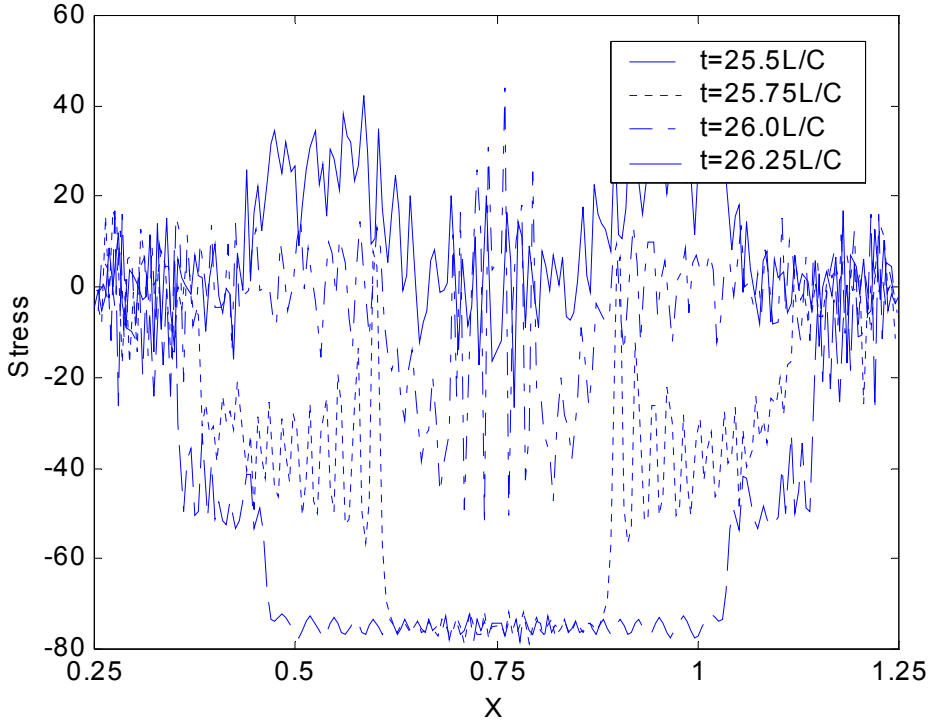

Figure 16. The changes in the stress profile corresponding to Figure 15, with Np=100 for each bar.

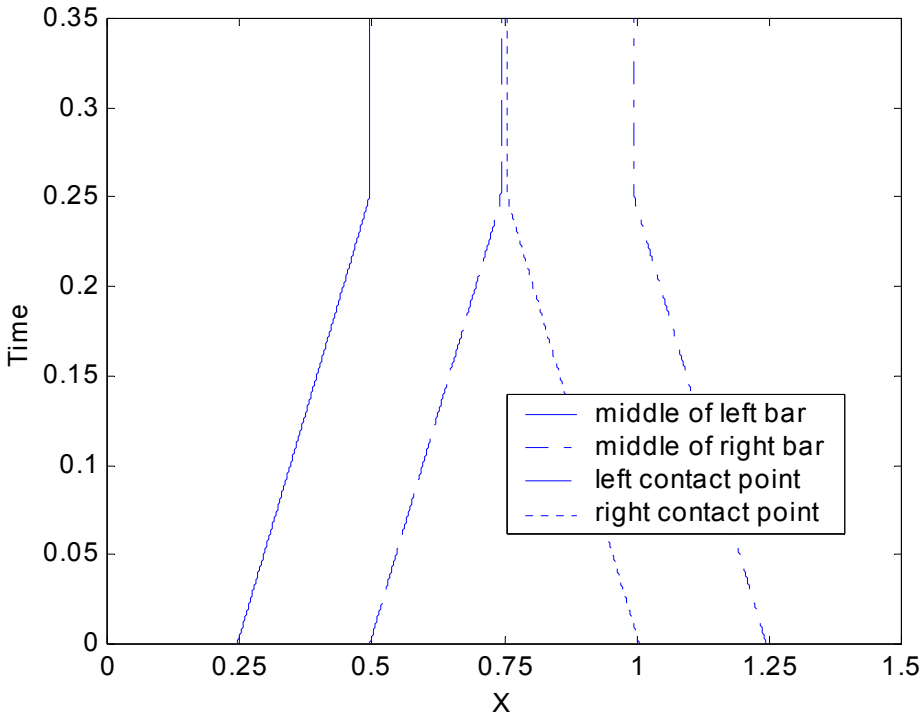

Figure 17. The impact between two elastic-perfect plastic bars (Np=50 for each bar), the distance between which is 0.5 at t=0.

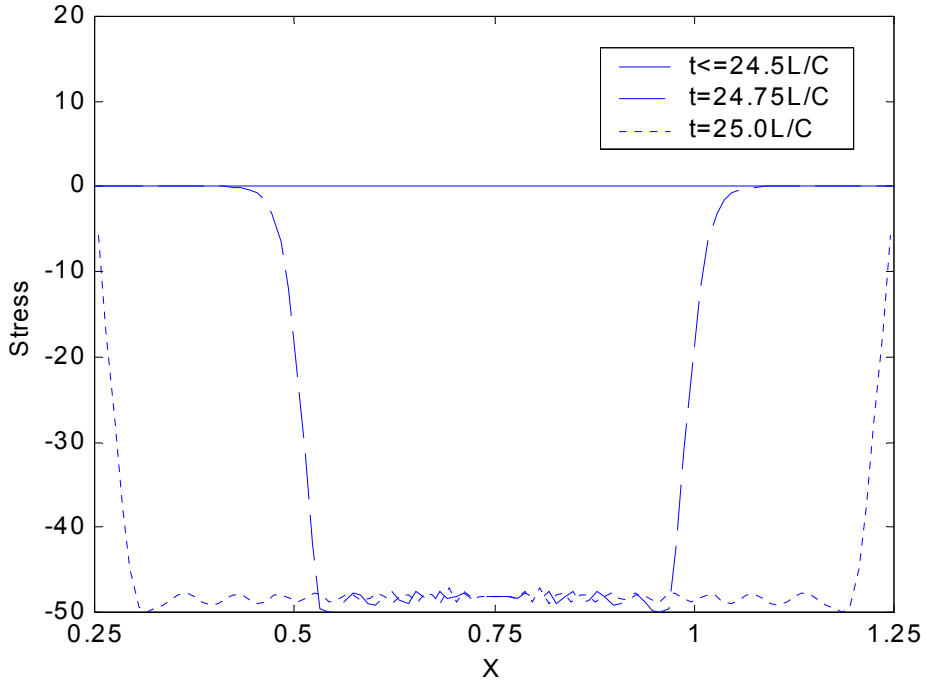

Figure 18. The changes in the stress profile corresponding to Figure 17.

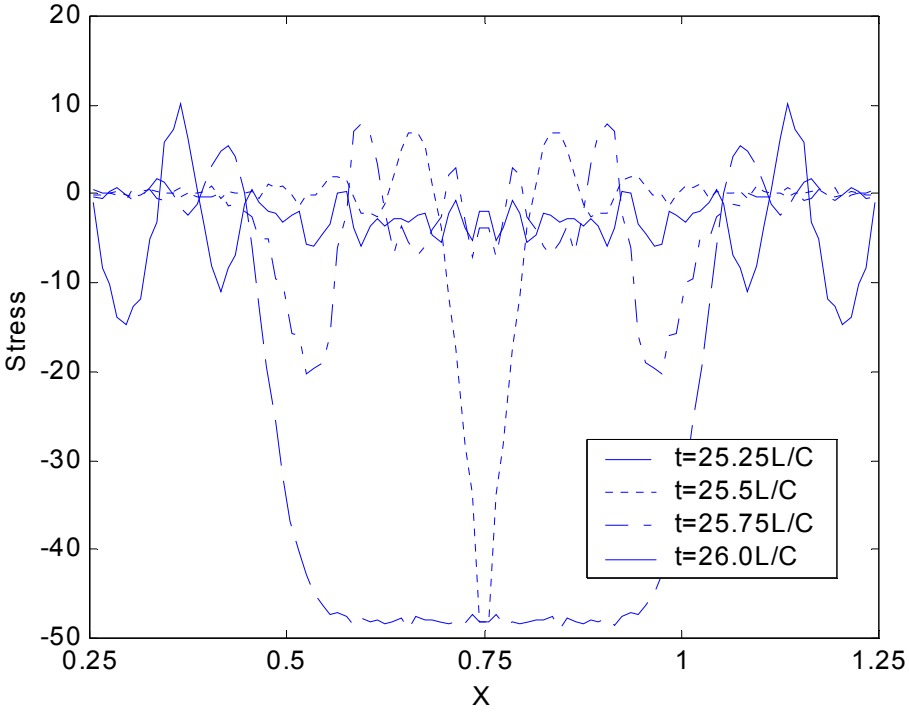

Figure 19. The continuation of Figure 18.

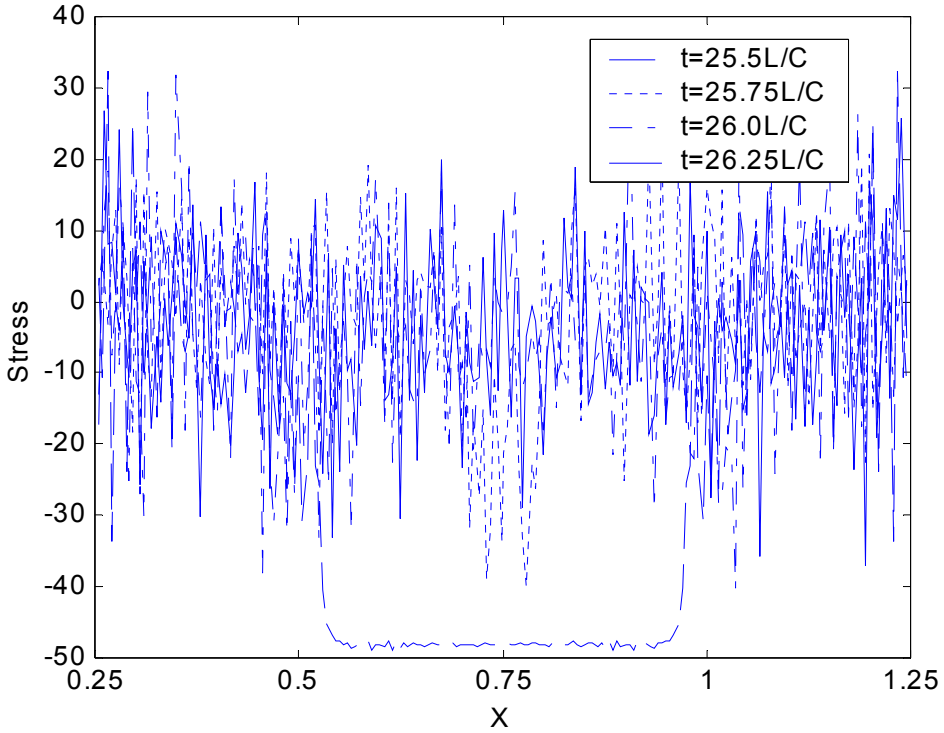

Figure 20. The changes in the stress profile corresponding to Figure 19, with Np=100 for each bar.

Distribution

EXTERNAL DISTRIBUTION

Zhen Chen
Dept. of Civil Engineering
E2509 Engineering Bldg. East
Columbia, MO 65211

G. Filbey
Army Research Laboratory,
AMSRL-WM-TA
Aberdeen Proving Ground, MD 21005-5066

Gordon Johnson
MN11-1614
Alliant Techsystems, Inc.
600 2nd Street NE
Hopkins, MN 55343-8384

Patrick McMurtry
University of Utah
Department of Mechanical Engineering
50 S. Central Campus Drive,
Room 2202
Salt Lake City, UT 84112-92MS 08

A.M. Rajendren
Army Research Laboratory,
AMSRL-MA-PD
Aberdeen Proving Ground MD 21005-5066

H. L. Schreyer
Department of Mechanical Engineering
University of New Mexico
Albuquerque, NM 87131

Deborah Sulsky
Department of Mechanical Engineering
University of New Mexico
Albuquerque, NM 87131

Los Alamos National Laboratory
Mail Station 5000
PO Box 1663
Los Alamos, NM 87545
Attn: Frank Addessio, MS B216
Attn: Jerry Brackbill, MS B216
Attn: D. L. Crane, MS P946
Attn: Gary A. Dilts, MS D413
Attn: Y. Horie, MS D413,
Attn: L. Libersky, MS D413, X-3

Sandia National Laboratories Internal

MS 0151 T.O. Hunter, 09100
MS 0310 P. Yarrington, 09230
MS 0310 G.S. Heffelfinger, 09209
MS 0316 J.B. Aidun, 09235
MS 0316 M.D. Rintoul, 09235
MS 0316 M.J. Stevens, 09235
MS 0321 W.J. Camp, 09200
MS 0525 T.V. Russo, 01734
MS 0751 L.S. Costin, 06117
MS 0751 A.F. Fossum, 06117
MS 0819 E.A. Boucheron, 09231
MS 0819 K.H. Brown, 09231
MS 0819 T.E. Voth, 09231
MS 0819 M.K. Wong, 09231
MS 0820 P.F. Chavez, 09232
MS0820 D.A. Crawford, 09232
MS 0820 M.E. Kipp, 09232
MS 0820 S.A. Silling, 09232
MS 0824 A.C. Ratzel, 09110
MS 0826 H.C. Edwards, 09131
MS 0826 W.L. Hermina, 09113
MS 0826 J.R. Stewart, 09131
MS 0826 J.D. Zepper, 09131
MS 0835 S.N. Kempka, 09141
MS 0835 J.S. Peery, 09142
MS 0836 M.R. Baer, 09100
MS 0836 E.S. Hertel, 09116
MS 0841 T.C. Bickel, 09100
MS 0847 S.W. Attaway, 09142
MS 0847 M.L. Blanford, 09121
MS 0847 S.N. Burchett, 09132
MS 0847 A.S. Gullerud, 09121
MS 0847 M. W. Heinstein, 09121
MS 0847 S.W. Key, 09121
MS 0847 J.A. Mitchell, 09121
MS 0847 H.S. Morgan, 09120
MS 0847 D. J. Segalman, 09124
MS 0847 J. W. Swegle, 09142
MS 0893 R.M. Brannon, 09123 **(5)**
MS 0893 R. S. Chambers, 09123
MS 0893 D.C. Hammerand, 09123
MS 0893 C.S. Lo, 09123
MS 0893 M.K. Neilsen, 09123
MS 0893 E.D. Reedy, 09123
MS 0893 W.M. Scherzinger, 09123
MS 0893 G.W. Wellman, 09123
MS 9042 M.L. Chiesa, 08727
MS 9042 J.J. Dike, 08727
MS 9042 J.M. Hruby, 08702
MS 9042 V.D. Revelli, 08727
MS 9161 E.P. Chen, 08726
MS 9161 P.A. Klein, 08726
MS 9405 D.J. Bammann, 08726
MS 9405 J.W. Foulk, 08726
MS 9405 M.F. Horstemeyer, 08726
MS 9405 D.A. Hughes, 08726
MS 1033 D.S. Drumheller, 06211
MS 1076 S.C. Hwang, 01745
MS 1152 M.L. Kiefer, 01642

Sandia National Laboratories Internal (cont'd)

MS 0612 Review and Approval Desk, 9612 **(1)**
for DOE/OSTI
MS 0899 Technical Library, 9616 **(2)**
MS 9018 Central Technical Files,
8945-1